Simulation of flow and transport phenomena in a polymer electrolyte fuel cell under low-humidity operation

Yun Wang, Chao-Yang Wang *

Department of Mechanical and Nuclear Engineering, Electrochemical Engine Center (ECEC), The Pennsylvania State University, University Park, PA 16802, USA

Abstract

Numerical simulations of a 50 cm^2 polymer electrolyte fuel cell (PEFC) with 36 channels are carried out to study the lateral transport of moisture and reactant between two neighboring channels with counter flow on the cathode side. Massive computations with 2.7 million computational elements are performed to capture the intricate electrochemical and transport phenomena in PEFC in three-dimensions. Two cases are examined and compared. One is under the common assumption that molecular diffusion dominates the species transport in the gas diffusion layer (GDL) and thus, the lateral convection effect is neglected. The other case is to include the flow and convection effects in the GDL using a realistic permeability of the porous GDL. Numerical results elucidate the mechanism and extent of internal humidification induced by lateral moisture diffusion. In addition, it is found that given the typical GDL, there exists a large pressure drop between two adjacent channels in counter flow, one flowing in from the inlet and the other flowing out to the outlet, causing severe reactant bypass between the two flow paths of reverse direction. The bypass results in reactant flow "short-circuit" and greatly diminishes the internal humidification benefit intended by the counter-flow design.
© 2005 Elsevier B.V. All rights reserved.

Keywords: Computational fuel cell dynamics; Polymer electrolyte fuel cells; Water management; Gas dynamics; Low humidity

1. Introduction

Due to development of perfluorosulfonic-acid membranes and the dramatic reduction in precious metal catalyst loading, the polymer electrolyte fuel cell (PEFC) has become a viable technology [1]. A PEFC consists of gas channels, gas diffusion layers (GDLs), and a proton-conductive membrane with platinum catalyst coated on the two surfaces, called the membrane electrode assembly (MEA). Gas channels are grooved in graphite or metal plates, where injected reactant streams are distributed for electrochemical reactions. Protons are produced from hydrogen oxidation in the anode catalyst layer, and pass through the membrane, carrying water molecules via electro-osmotic drag, to the cathode catalyst layer where

the oxygen reduction reaction (ORR) occurs, with water as the product.

Water management is a central issue in PEFC technology because high water content results in high proton conductivity of the membrane, thus decreasing ohmic voltage loss. Commonly, two methods are used to hydrate the membrane. One is to externally humidify inlet reactant gases. This strategy requires a humidifier, making it complex and expensive to be applied to portable or mobile systems. The other way is to make full use of water production inside a PEFC and humidify reactant gases internally. In the latter approach, Qi and Kaufman [2] proposed a counter-flow cathode flowfield design where an inlet gas channel is placed next to an outlet channel in hopes that the moist air in the outlet channel will help humidify the dry air in the inlet channel. Such a self-humidification process is of technological interest as it has the potential to feed dry reactants without external humidification. While cell polarization experiments

* Corresponding author. Tel.: +1 814 863 4762; fax: +1 814 863 4848.
 E-mail address: cxw31@psu.edu (C.-Y. Wang).

Nomenclature

a	effective catalyst area per unit volume (m^2/m^3)
A	superficial electrode area (m^2)
C_k	molar concentration of species k (mol/m^3)
D	mass diffusivity of species (m^2/s)
F	Faraday's constant, 96,487 C/equivalent
i_0	exchange current density (A/m^2)
I	current density (A/cm^2)
j	transfer current (A/cm^3)
K	permeability (m^2)
n	the direction normal to the surface
n_d	electro-osmotic drag coefficient (H_2O/H^+)
p	pressure (Pa)
R	gas constant (8.134 J/mol K)
s	stoichiometric coefficient in electrochemical reaction
S	source term in transport equations
t	time (s)
T	temperature (K)
$\vec{u}$	velocity vector (m/s)
U_o	open circuit potential (V)
V_{cell}	cell potential (V)
X	mole fraction

Greek

α	transfer coefficient or net water transport co-efficient per proton
ε	porosity
ϕ	phase potential (V)
η	surface overpotential (V)
κ	ionic conductivity (S/m)
λ	membrane water content
μ	viscosity (kg/m s)
σ	electronic conductivity (S/cm)
ρ	density (kg/m^3)
τ	shear stress (N/m^2, or tortuosity factor)
ξ	stoichiometric flow ratio

Superscripts and Subscripts

a	anode
avg	average
c	cathode
e	electrolyte
eff	effective value
g	gas phase
in	inlet
k	species
m	membrane
o	standard condition, 273.15 K and 101.3 kPa (1 atm)
ref	reference
s	solid phase of electrode
sat	saturate value
w	water

have been reported by Qi and Kaufman [2] for this flowfield design, a fundamental understanding of the complex transport phenomena uniquely present in this flow configuration is absent.

Mathematic models, describing detailed physico-chemical processes and coupling transport equations with electrochemical kinetics, are an important tool to aid in fundamental understanding of relevant phenomena in PEFCs. To date, mathematic models have been developed from the simple one-dimensional [3–5], two-dimensional [6,7] to the complex three-dimensional models. Springer et al. [4,5] presented a detailed description of water behavior in the membrane and experimentally measured the water-diffusion coefficient, electro-osmotic drag coefficient and membrane proton conductivity as functions of membrane water content. Fitted curves were incorporated into their one-dimensional model to capture water transport phenomena in the membrane via molecular diffusion and electro-osmotic drag. Fuller and Newman [6] considered two-dimensional MEA in the through-plane and flow directions operating on reformed methanol. Water management, thermal management and utilization of fuel were examined in detail.

A comprehensive non-isothermal, three-dimensional model was developed by Berning et al. [8]. They simulated a half of a single channel to study the temperature distribution. However, their model ignored the membrane-electrode assembly, thus not capturing the transport and electrochemical mechanisms in these vital components of PEFCs. The same assumption also existed in the model of Dutta et al. [9,10]. An important contribution of Dutta's work is to simulate a fuel cell with 20-branch serpentine channels. However, only about 200,000 grid points were employed in the simulations, raising the concern of grid dependence and numerical inaccuracy. In addition, the governing equations were employed only in the gas channels and GDLs, with the MEA excluded. Water transport in the MEA was analytically modeled based on the approximations of constant transport properties, and the diffusion flux through the membrane was calculated based on the difference of water concentrations in the two catalyst layers. In contrast, Wang and co-workers [11–15] presented a single-domain model, including detailed mechanisms in the MEA, such as electrolyte potential, current and water distributions in the membrane as well as catalyst layers. Thus, their model is chosen for this study of internal humidification and membrane hydration.

The goal of this paper is to investigate the internal humidification phenomenon through the simulations of a $50\,cm^2$ PEFC with counter flow in the cathode flowfield. The geometry of the fuel cell is similar to the one in the work by Qi and Kaufman [2] except that a complete PEFC with 36 channels is considered. We expand upon the model of Um et al. [11] and numerically implement it into Star-CD®, a commercial computational fluid dynamics (CFD) software package, based on its user coding capability.

2. Numerical Model

Fig. 1(a) shows the computational domain of the double-path PEFC with 36 channels under consideration. There are two parallel branches of 18 channels in a serpentine fashion on each side. Anode-side and cathode-side flow channels are symmetric and properly aligned on top of each other. Fig. 1(b) shows part of the mesh near inlet and outlet areas. Finer grids are used to capture the transport phenomena in channel U-turns and inlet regions. Detailed mesh in the through-plane direction of the MEA is plotted in Fig. 1(c). Three-dimensional mesh is necessary to capture the important electrochemical and transport mechanisms occurring in the MEA and GDL. These include species transport in the through-plane direction, flow and reactant consumption in the flow direction, and gas flow and water transport in the in-plane direction in the GDL over the land separating two neighboring channels. Fig. 1(d) schematically shows the top view of the computational domain of double-path PEFC with 36 channels and the positions of inlets and outlets. In order to focus on the effects of internal humidification, we consider counter flow only in the cathode flowfield and use a common co-flow pattern in the anode one. In addition, dry air is fed into Channels 1 and 35 on the cathode, and fully-humidified hydrogen is injected into Channels 1 and 2 for the anode. The mid-length cross-section of the fuel cell is typically selected to show the detailed profiles of flow and transport parameters. To distinguish the two flow paths in the cathode side, the one with Channel 1 as the inlet is defined as Path 1 while the other one starting from the other end is Path 2. The PEFC geometry is shown in Table 1.

Table 1
Geometrical and physical parameters

Quantity	Value
Gas channel depth (mm)	1.0
Gas channel width (mm)	1.0
Shoulder width (mm)	1.0
Diffusion layer thickness (mm)	0.3
Catalyst layer thickness (mm)	0.01
Membrane (N112) thickness (mm)	0.051
Fuel cell height/length (mm)	72.0/72.0
Anode/cathode pressure, p (atm)	2.0/2.0
Reference current density, I_{ref} (A/cm^2)	1.0
Stoichiometric ratio ξ in the anode/cathode	2.0/2.0
RH of anode/cathode inlet (%)	100/0
Temperature of fuel cell, T (K)	353
Porosity of the GDL, ε [18]	0.6
Porosity of catalyst layers, ε_g [18]	0.4
Volume fraction of ionomer in catalyst layers, ε_m [18]	0.26
Permeability of the GDL, K (m^2)[18]	10^{-12}
H$_2$ diffusivity in anode gas at standard condition, $D_{o,H_2,a}$ (m^2/s) [22]	1.1028×10^{-4}
H$_2$O diffusivity in anode gas at standard condition, $D_{o,w,a}$ (m^2/s) [22]	1.1028×10^{-4}
O$_2$ diffusivity in cathode gas at standard condition, $D_{o,O_2,c}$ (m^2/s) [22]	3.2348×10^{-5}
H$_2$O diffusivity in cathode gas at standard condition, $D_{o,w,c}$ (m^2/s) [22]	7.35×10^{-5}

2.1. Model equations

The single-phase PEFC model consists of non-linear, coupled partial differential equations describing the conservation of mass, momentum, species and charge with electrochem-
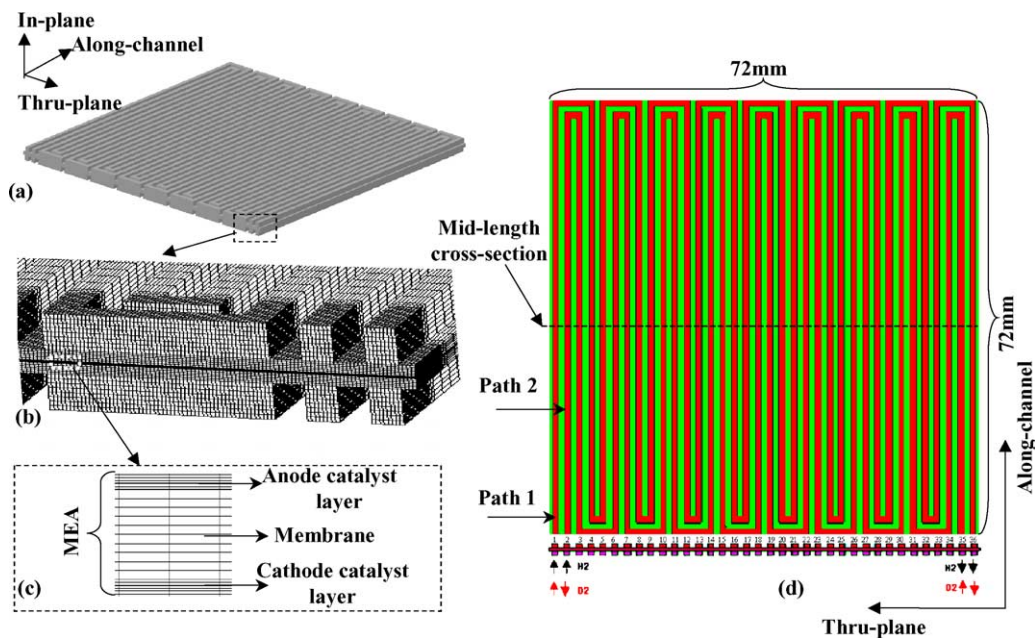

Fig. 1. (a)–(d) Geometry, grids and top view of the computational domain of the double-path PEFC with 36 channels.

ical reactions. The equations can be written, in the vector form, as [11]:

Continuity conservation : $\qquad \nabla \cdot (\rho \vec{u}) = 0 \qquad$ (1)

Momentum conservation :

$$\frac{1}{\varepsilon^2} \nabla \cdot (\rho \vec{u} \vec{u}) = -\nabla p + \nabla \cdot \tau + S_u \qquad (2)$$

Species conservation : $\qquad \nabla \cdot (\vec{u} C_k) = \nabla \cdot (D_k^{\text{eff}} \nabla C_k) + S_k$

$$(3)$$

Charge conservation : $\qquad \nabla \cdot (\kappa^{\text{eff}} \nabla \phi_e) + S_e = 0 \qquad$ (4)

where ρ, $\vec{u}$, p, C_k and ϕ_e, respectively, denote the density, superficial fluid velocity vector, pressure, mole fraction of species k and electrolyte potential. The species considered are hydrogen, oxygen and water. In Eqs. (1) and (2), use has been made of a constant-flow assumption in which the fluid density is constant and the mass source/sink in the continuity equation

is ignored. This constant-flow approximation has proved to be valid under common PEFC operations [16]. Source terms, electrochemical properties and physical properties, identified for various regions of a fuel cell, are listed in Tables 2–4, respectively.

In the GDL, a small value of permeability K will result in a large source term S_u in Eq. (2), turning Eq. (2) into the

Table 2
Source terms for the conservation equations in each region

	S_u	S_k	S_ϕ
Gas channels	0	0	–
Diffusion layers	$S_u = -\dfrac{\mu}{K}\vec{u}$	0	0
Catalyst layers	$S_u = -\dfrac{\mu}{K}\vec{u}$	$S_k = -\nabla \cdot \left(\dfrac{n_d}{F} i_e\right) - \dfrac{s_k j}{n F}$	$S_\phi = j$
Membrane	$S_u = -\dfrac{\mu}{K}\vec{u}$	0	0

Note: n_d is the electro-osmotic drag coefficient for water. For H_2 and O_2, $n_d = 0$.

Table 3
Electrochemical properties

Description	Anode	Cathode
Transfer current density, j (A/m^3)	$ai_{0,a}\left(\dfrac{C_{H_2}}{C_{H_2,\text{ref}}}\right)^{1/2}\left(\dfrac{\alpha_a + \alpha_c}{RT} \cdot F \cdot \eta\right)$	$-ai_{0,c}\left(\dfrac{C_{O_2}}{C_{O_2,\text{ref}}}\right) e^{\left(-\frac{\alpha_c F}{RT} \cdot \eta\right)}$
Surface overpotential, η (V)	$\phi_s - \phi_e - U_o$ (with $\phi_s = 0$)	$\phi_s - \phi_e - U_o$ (with $\phi_s = V_{\text{cell}}$)
Equilibrium potential, U_o (V)	0	$1.23 - 0.9 \times 10^{-3}(T - 298)$
Exchange current density x reaction surface area, ai_0 (A/m^3)	1.0×10^9	10000
Transfer coefficient, α	$\alpha_a + \alpha_c = 2$	$\alpha_c = 1$

Table 4
Physical and transport properties

Quantity	Value
Water activity, a [4]	$a = \dfrac{C_w RT}{p^{\text{sat}}}$ $\log_{10} p^{\text{sat}} = -2.1794 + 0.02953(T - 273.15) - 9.1837 \times 10^{-5}(T - 273.15)^2 + 1.4454 \times 10^{-7}(T - 273.15)^3$
Water content in membrane, λ [4]	$\lambda = \begin{cases} 0.043 + 17.81a - 39.85a^2 + 36.0a^3 & \text{for} \quad 0 < a \leq 1 \\ 14 + 1.4(a - 1) & \text{for} \quad 1 \leq a \leq 3 \end{cases}$
Ionic conductivity of membrane, κ (S/m) [4]	$(0.005139\lambda - 0.00326) \exp\left[1268\left(\dfrac{1}{303} - \dfrac{1}{T}\right)\right]$
H_2O diffusivity in membrane, D_w^m (m^2/s) [19]	$D_w^m = \begin{cases} 3.1 \times 10^{-3}\lambda(e^{0.28\lambda} - 1) \cdot e^{[-2346/T]} & \text{for} \quad 0 < \lambda \leq 3 \\ 4.17 \times 10^{-4}\lambda(1 + 161e^{-\lambda}) \cdot e^{[-2346/T]} & \text{otherwise} \end{cases}$
Electro-osmotic drag coefficient, n_d [20]	$n_d = \begin{cases} 1.0 & \text{for} \quad \lambda \leq 14 \\ \dfrac{1.5}{8}(\lambda - 14) + 1.0 & \text{otherwise} \end{cases}$
Membrane density, ρ (kg/m^3) [21]	$\rho = \dfrac{1.98 + 0.0324\lambda}{1 + 0.0648\lambda} \times 10^3$
H_2/O_2 diffusivity in membrane, $D_{H_2}^m/D_{O_2}^m$ (m^2/s) [3]	$2.59 \times 10^{-6}/1.22 \times 10^{-6}$
Gas diffusivity in porous media, D^{eff} (m^2/s)	$D^{\text{eff}} = \varepsilon^{1.5} D$
Diffusivity in gas, D (m^2/s) [22]	$D_o\left(\dfrac{T}{353}\right)^{3/2}\left(\dfrac{1}{p}\right)$
Viscosity of anode/cathode gas, μ (kg/m s) [23]	$\mu = 9.88 \times 10^{-6}X_{H_2} + 1.12 \times 10^{-5}X_{H_2O} + 2.01 \times 10^{-5}X_{N_2} + 2.3 \times 10^{-5}X_{O_2}$

Darcy's law for porous media:

$$\nabla p = \frac{\mu}{K} \vec{u} \tag{5}$$

In addition, notice that the present model is a single-phase approach in which the total water amount is tracked without distinguishing liquid water from water vapor. Such a single-phase model is valid generally under the condition that the liquid volume fraction is low or liquid droplets are small to form a mist flow. This approach is particularly well suited for the present study since only the low-humidity operation is concerned.

2.2. Boundary conditions

Eqs. (1)–(4) form a complete set of governing equations with eight unknowns: $\vec{u}$, p, C_{H_2}, C_{O_2}, C_{H_2O} and ϕ_e. Their corresponding boundary conditions are specified as follows.

2.2.1. Flow inlet boundaries
The inlet velocity $\vec{u}_{in}$ in a gas channel is expressed by the respective stoichiometric flow ratio, i.e. ξ_a or ξ_c, defined at a reference current density, I_{ref}, as:

$$\xi_a = \frac{C_{H_2} \rho_a u_{in,a} A_a}{\frac{I_{ref} A}{2F}} \quad \text{and} \quad \xi_c = \frac{C_{O_2} \rho_c u_{in,c} A_c}{\frac{I_{ref} A}{4F}} \tag{6}$$

where A_a and A_c are the flow cross-sectional areas of the anode and cathode gas channels, respectively. The inlet molar concentrations are determined by the inlet pressure and humidity according to the ideal gas law.

2.2.2. Outlet boundaries
Fully developed or no-flux conditions are applied:

$$\frac{\partial \vec{u}}{\partial n} = 0, \qquad \frac{\partial C_k}{\partial n} = 0, \qquad \frac{\partial \phi_e}{\partial n} = 0 \tag{7}$$

2.2.3. Wall
No-slip and impermeable velocity condition and no-flux condition are applied:

$$\vec{u} = 0, \qquad \frac{\partial C_k}{\partial n} = 0, \qquad \frac{\partial p}{\partial n} = 0, \qquad \frac{\partial \phi_e}{\partial n} = 0 \tag{8}$$

2.3. Numerical procedure

The conservation equations are solved by Star-CD software with SIMPLE algorithm [17], using a parallel computational methodology for a Linux PC cluster. The source terms and physical properties are incorporated in the user codes. Cell voltage is prescribed and local current density distribution is computed in all simulations to be presented in this work. Alternatively, an average current density can be prescribed and the cell voltage is computed if the electron transport equation is included, as shown in [15]. After grid-independence study, about 2.7 million computational elements ($44 \times 100 \times 576$) were determined to be necessary to

capture fine details of flow and transport phenomena in this PEFC configuration. A simulation typically requires about 100 iterations and takes nearly 5 h on 9 nodes of 1.4 GHz AMD Athelon Thunderbird CPU and 512MB DDR SDRAM.

3. Results and discussion

Two cases are compared in our study, in Case 1, we assume there is no velocity in the GDL, thus species transport is dominated by diffusion. The other one, Case 2, is to apply the Darcy's law in the GDL based on its permeability and explore the convection effect on internal humidification additionally.

Fig. 2 shows the local velocity distribution at the mid-depth of the cathode gas channels for Case 1. The grid is much finer at the U-turns, inlet and outlet, in order to capture the complex flow in these locations, such as flow recirculation. From the inlet of Channel 1, the gas velocity profile undergoes a change from the uniform flow to fully-developed flow which can be seen in Channel 4 before the U-turn. A similar parabolic profile velocity is displayed at Channel 2, which is the outlet channel of Path 2. In the gas channel, the convection dominates the mass transport, and species is distributed down the flow paths.

Fig. 3 shows the distributions of average O_2 and H_2O concentrations in the cathode gas channel of each flow path for Case 1. O_2 concentration is seen to decrease along the channels from the two inlets, due to the oxygen reduction reaction. The concentration difference between the two flow paths is maximum in the inlet and outlet areas and diminishes to zero in the middle of the cell. In addition, O_2 displays a nearly symmetric profile between the two flow paths, indicating that nearly equal amount of O_2 is consumed along each path.

In contrast, H_2O concentration increases along the channel from the inlet to outlet due to water production of ORR. Furthermore, H_2O concentration exhibits asymmetric distri-
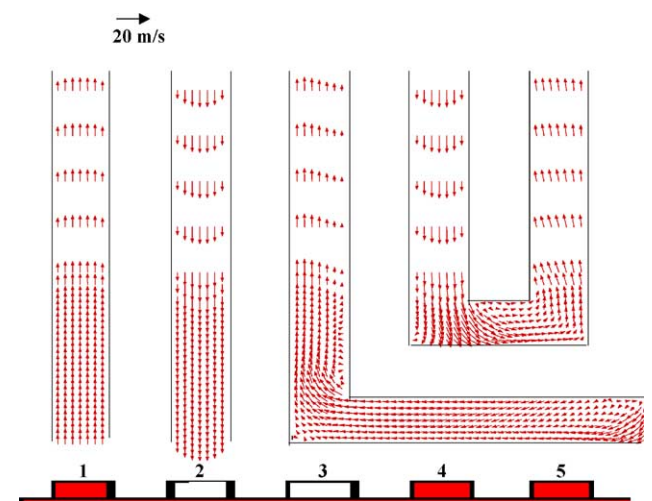

Fig. 2. Velocity distribution at the mid-depth of the cathode gas channel without convection in the GDL.
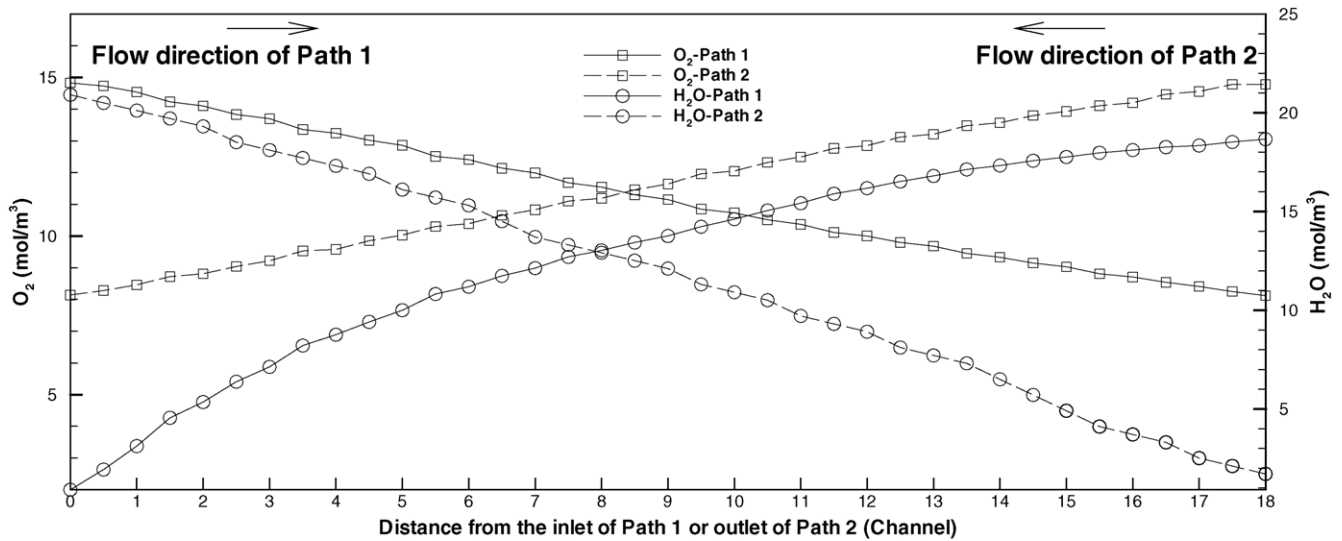
Fig. 3. Average O_2/H_2O concentrations in the cathode gas channel for each flow path without convection in the GDL at $V_{cell} = 0.65$ V and $I_{avg} = 0.91$ A/cm^2.

butions between the two flow paths. This is due to the effect of anode co-flow pattern where humidified H_2 is fed into Channels 1 and 2 from same end of the cell. In addition, there exists great difference of water concentration between the two flow paths in the inlet or outlet areas, where internal humidifica-

tion is expected to occur due to lateral diffusion through the porous GDL.

Details of the lateral transport of H_2O and O_2 between two adjacent channels in the different flow paths are shown in Fig. 4(a) and (b), respectively. The cross-section is taken
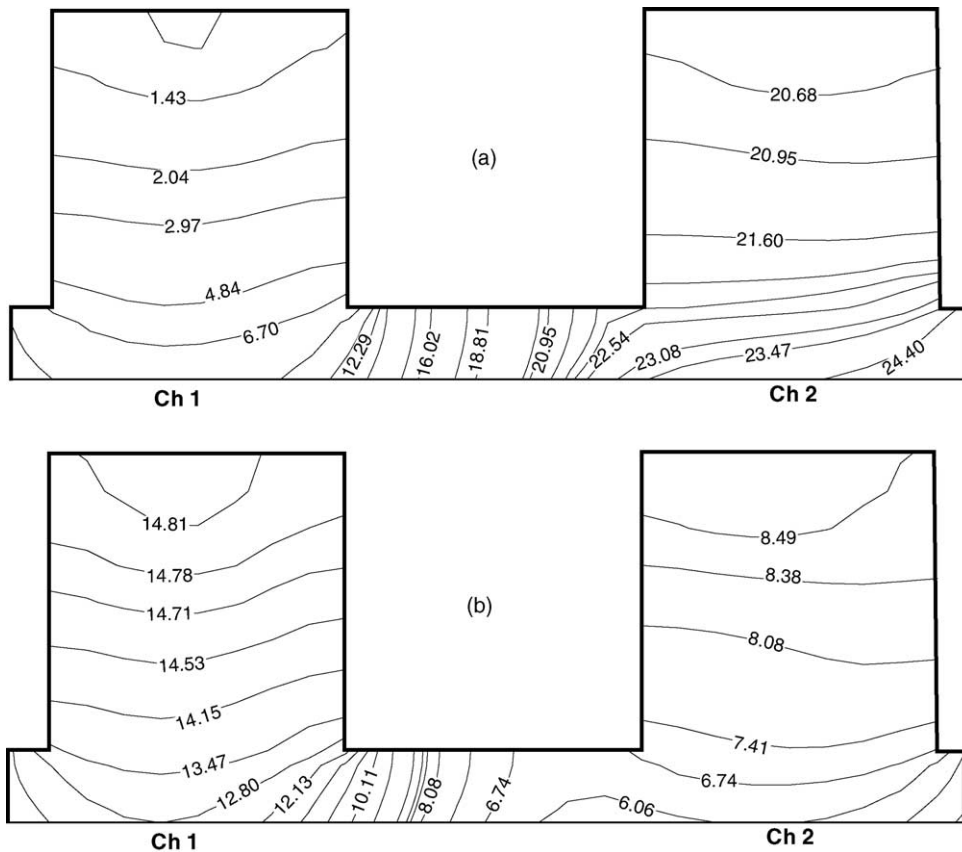
Fig. 4. (a) H_2O and (b) O_2 distributions, respectively, in the cathode at the mid-length cross-section between Channels 1 and 2 without convection in the GDL at $V_{cell} = 0.65$ V and $I_{avg} = 0.91$ A/cm^2.
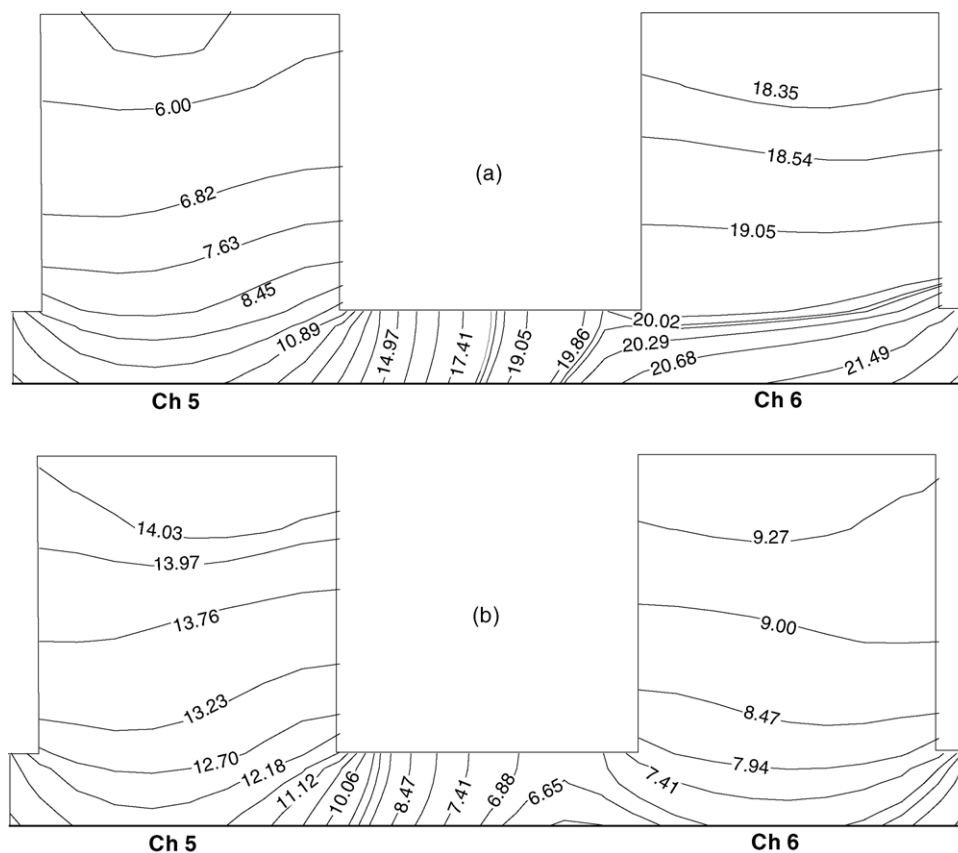
Fig. 5. (a) H_2O and (b) O_2 distributions, respectively, in the cathode at the mid-length cross-section between Channels 5 and 6 without convection in the GDL at $V_{cell} = 0.65$ V and $I_{avg} = 0.91$ A/cm^2.

on the cathode side at the mid-length of the fuel cell between Channels 1 and 2 under $V_{cell} = 0.65$ V and $I_{avg} = 0.91$ A/cm^2. A clear gradient in the water concentration towards the dry inlet channel (Channel 1) is evident. Fig. 4(b) shows O_2 concentration is lowest in the GDL under the land. This is due to the ORR under the land and the fact that the thin GDL limits the O_2 supply.

Fig. 5(a) and (b) display the corresponding H_2O and O_2 distributions, respectively, between Channels 5 and 6 under the same conditions as in Fig. 4. Fig. 5(a) shows that there also exist dramatic concentration differences between these two channels both for water and oxygen. Similar to Fig. 4(a), the highest concentration of H_2O appears under the land. Fig. 5(b) also indicates virtually no O_2 exchange between the two channels.

The reason why there is no direct water exchange between the two channels in Figs. 4 and 5 is due to local water production under the land. If there were no such water source, water vapor would diffuse from the humid channel to the dry one under the concentration difference. However, water source under the land raises the local water concentration even beyond the wet channel nearby, thus preventing water diffusion between the two channels. Nonetheless, a larger portion of product water is laterally removed into the drier gas channel, so there is a limited extent of internal humidification.

Fig. 6(a) and (b) show H_2O and O_2 distributions, respectively, in the cathode side between Channels 35 and 36. In this location, different to Figs. 4 and 5, water concentration under the land is lower than the humid Channel 36, so a lateral water flux induced by diffusion occurs through the GDL between the two channels. Simultaneously, water produced under the land also enters the dry Channel 35. This more beneficial effect of internal humidification occurs in the very last channel towards the exit. Fig. 6(b) shows that there is still no O_2 exchange between the two channels. Rather, O_2 needed for the electrochemical reaction under the land is supplied from both channels.

The effect of internal humidification is shown quantitatively in Fig. 7, which indicates the water flux across the two surfaces of the cathode GDL along the mid-length cross-section for Case 1. The areas under the curves, i.e. the integrals of the curves, represent the amount of water across each face of the GDL per unit length. Due to no water production in the GDL, the area between the two curves across the two surfaces of the GDL represents the net water flux along the lateral direction. It can be seen that the amount of water into the gas channel is almost twice that across the interface between the catalyst layer and GDL under Channel 1, while the water fluxes across the two surfaces of the GDL are almost equal under Channel 2. The different amount of prod-
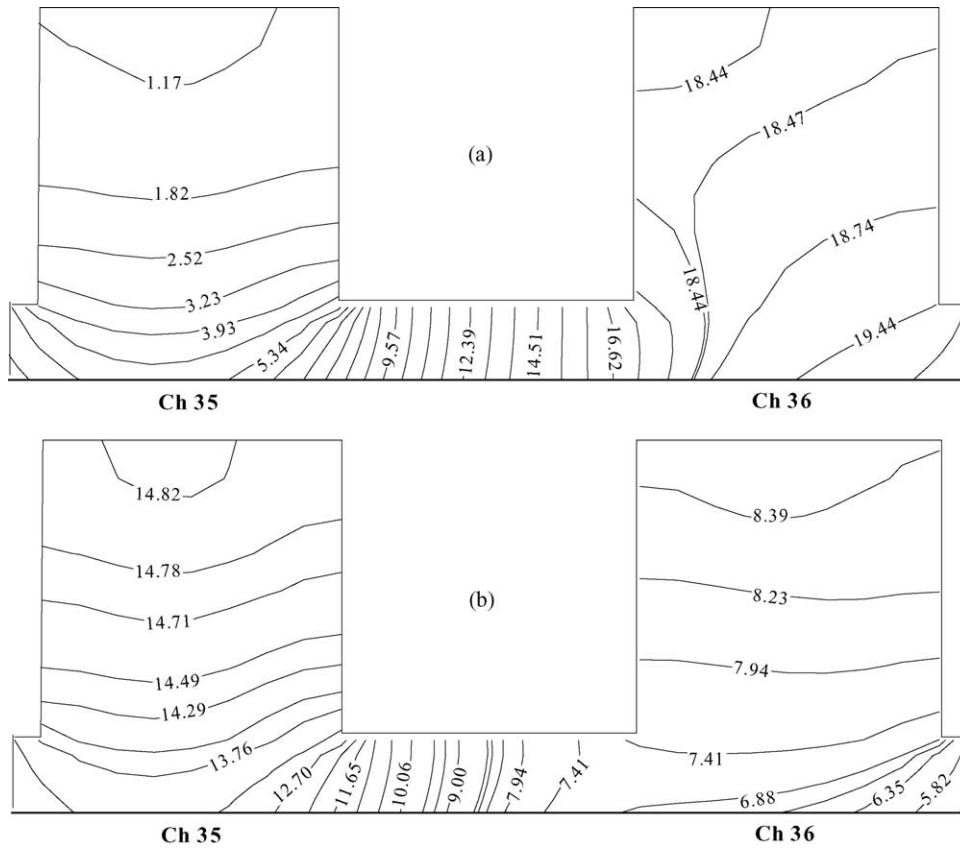
Fig. 6. (a) H$_2$O and (b) O$_2$ distributions, respectively, in the cathode at the mid-length cross-section between Channels 35 and 36 without convection in the GDL at $V_{cell} = 0.65$ V and $I_{avg} = 0.91$ A/cm^2.

uct water captured by the inlet Channel 1 and outlet Channel 2 indicates that internal humidification exists and has a significant effect on humidifying the dry inlet flow. The same trend also exists in the channels close to the air inlet such as Channels 4, 5, 34 and 35, and the channels close to the exhaust outlet such as Channels 3, 6, 33 and 36. In Channel 36, there exists a negative flux across the front face of the GDL, which means that water diffuses from Channel 36 into the GDL and is transported laterally through the GDL to Channel 35. Similar phenomenon also appears in the outlet
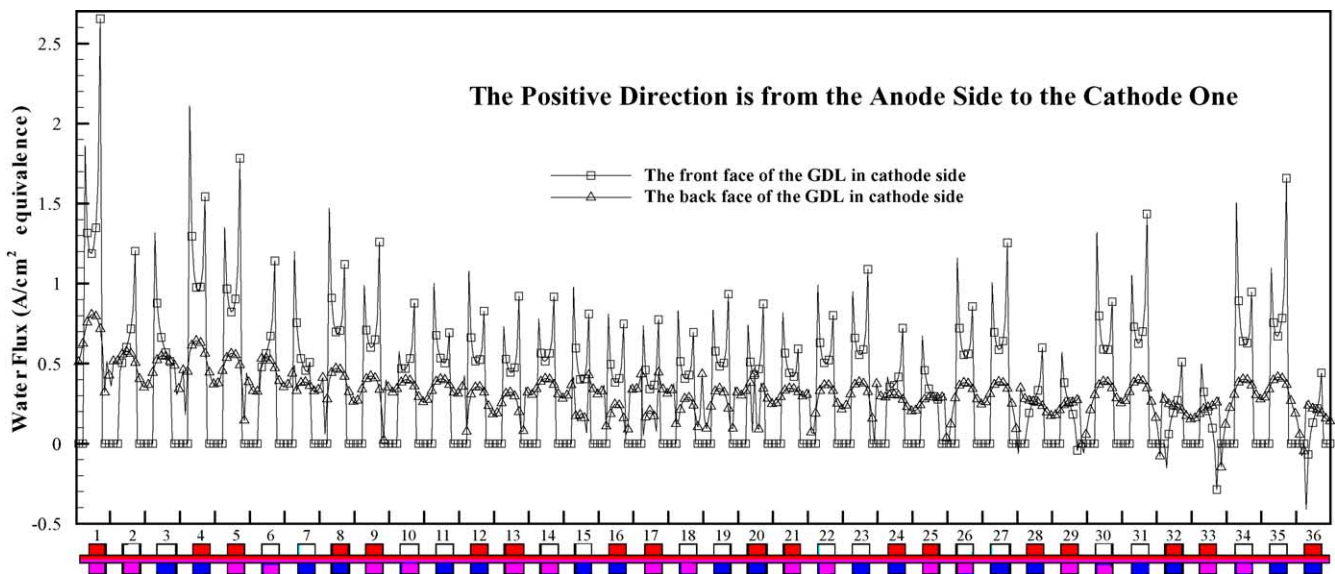
Fig. 7. Water flux across surfaces of the cathode GDL at the mid-length cross-section without convection in the GDL under $V_{cell} = 0.65$ V and $I_{avg} = 0.91$ A/cm^2.
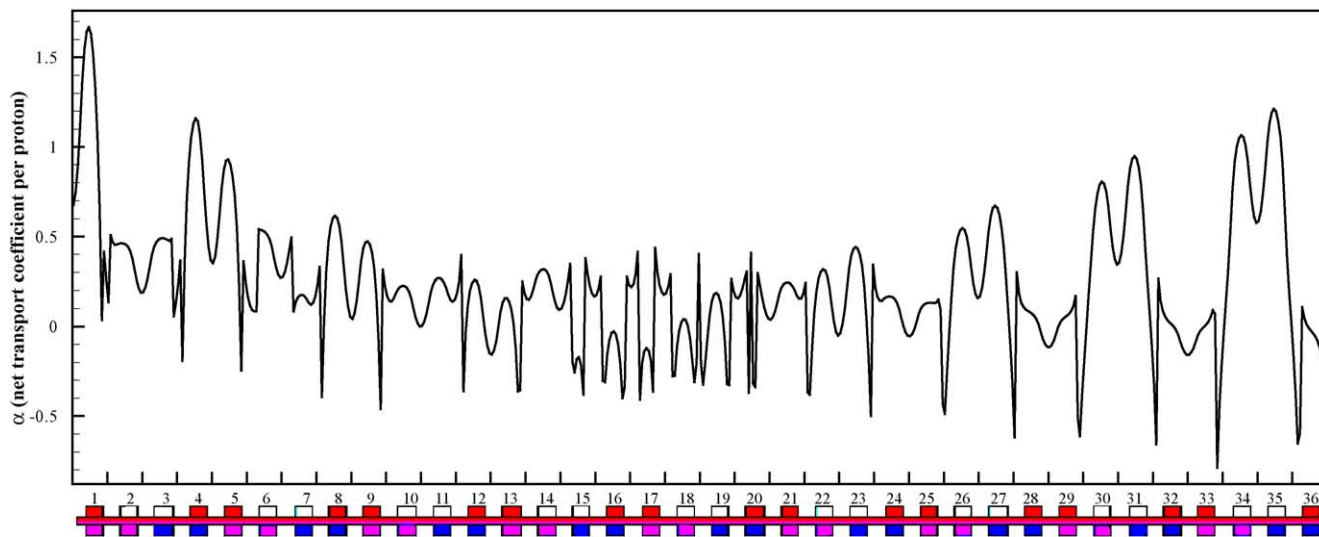
Fig. 8. Net water transport coefficient per proton at the mid-length cross-section without convection in the GDL at $V_{cell} = 0.65$ V and $I_{avg} = 0.91$ A/cm^2.

channels, such as Channels 32 and 33. However, the amount of water transported between the two neighboring channels remains very small. In addition, the highly oscillatory nature of these surface water fluxes is indicative of the complex water transport phenomena occurring in the flow field and thus calls for a fine mesh to resolve sharp gradients in the lateral direction.

Fig. 8 shows the distribution of net water transport coefficient per proton at the same cross-section. The α-value reflects the combined effect of electro-osmotic drag and back diffusion of water, with positive values being water transported from the anode to cathode. It is highly dependent on the location and varies from -0.5 to 1.5. The peak values appear near the cathode dry inlet channels, Channels 1, 4, 34

and 35, while near the cathode outlet channels, such as Channels 2, 3 and 36, α is less than unity because of strong back diffusion. In addition, under the land, such as the one between Channels 33 and 34, α dramatically changes from a positive to a negative value. This can be explained by water accumulation under lands. Furthermore, Fig. 8 clearly indicates that α is highly dependent upon the local conditions.

In Case 1, the velocity in the GDL has been ignored and the species transport is only by diffusion. However, velocity will be induced by the pressure gradient following the Darcy's law in porous media. Fig. 9 shows the gas pressure distribution in the cathode GDL at the mid-length cross-section when lateral gas flow is considered (i.e. for Case 2). It is seen that there exists a large pressure drop in the GDL between the adjacent
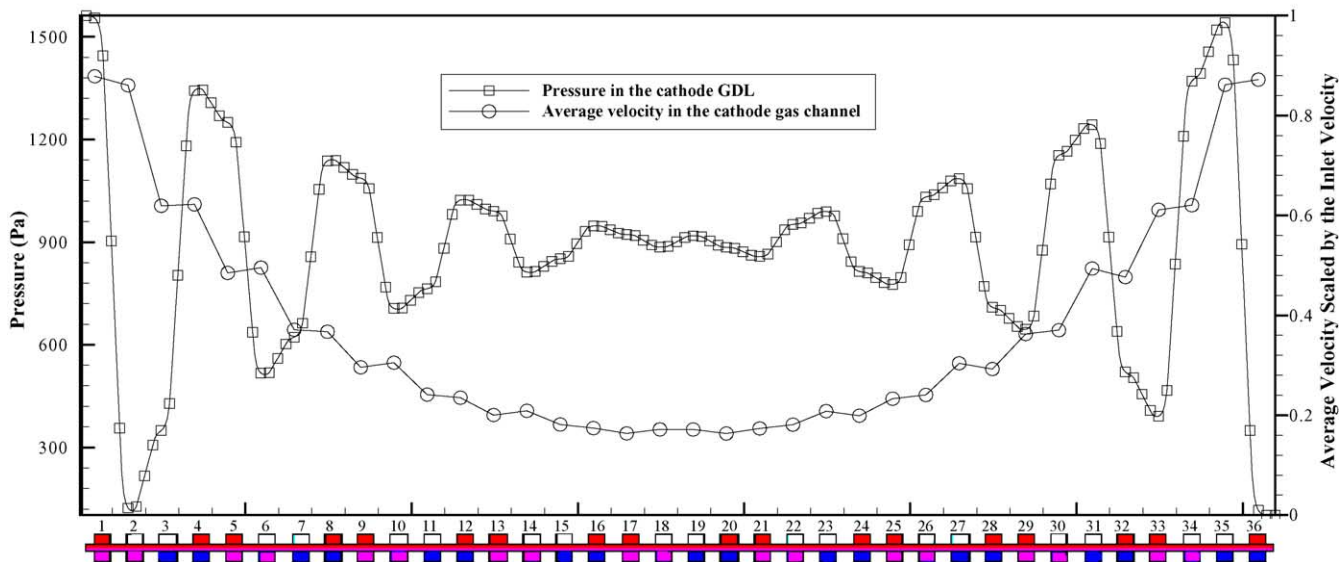

Fig. 9. Pressure distribution in the cathode GDL and average velocity scaled by the cathode inlet velocity at the mid-length cross-section with convection in the GDL.

channels in different flow paths at the two ends of the fuel cell. Between Channels 1 and 2, c.a. 1.5 kPa pressure difference is present. According to the Darcy's law, Eq. (5), and using the GDL permeability of 10^{-12} m^2, one obtains a lateral velocity of about 0.15 m/s in the GDL from the dry Channel 1 to wet Channel 2. As a result, there is a certain amount of inlet fresh air bypassing through the GDL and directly flowing into the channel in the other flow path towards the exit. This gas bypass, or "short circuit", greatly reduces the reactant utilization in the cell.

To quantify the bypass, average gas velocity in the cathode gas channels is also presented in Fig. 9. It can be seen that bypass causes severe leakage of injected flow. For Path 1, from the inlet Channel 1 to the middle of the fuel cell, e.g. Channel 17, the mass of flow in the channel decreases by about 80%. From the middle to the outlet Channel 36, the flow acquires four times mass from the other flow path.

Besides severe gas bypass, the lateral convection from the dry inlet channel to the wet outlet channel opposes to water diffusion, thus greatly diminishing the self-humidification benefit. The effect of convection on species transport is indicated in Fig. 10, which superposes H$_2$O/O$_2$ concentration contours with the velocity vector plot in the cathode side between Channels 1 and 2. It is seen that about 0.1 m/s velocity in the porous GDL is induced by the pressure difference between the two channels, in consistency with the estimate made earlier. If we define the Peclet number as a parameter to measure the relative strength of convection to molecular diffusion, then:

$$\text{Pe} = u \frac{\delta_{\text{land}}}{D_{\text{GDL}}^{\text{eff}}} \tag{9}$$

For $D^{\text{eff}} \approx 10^{-5}$ m^2/s and $\delta_{\text{land}} = 0.001$ m, Pe is about 10, demonstrating that convection is dominant in the lateral species transport through the GDL. As a result, the bypass flow significantly offsets the internal humidification induced by diffusion. In addition, bypass loses fresh air of higher concentration in O$_2$ to the outlet channel towards the exit from the fuel cell.

Similarly, strong bypass exists between other inlet and outlet channels, as shown in Fig. 11 between Channels 5 and 6. The magnitude of the lateral velocity is reduced to about 0.05 m/s but convection still dominates the species transport.
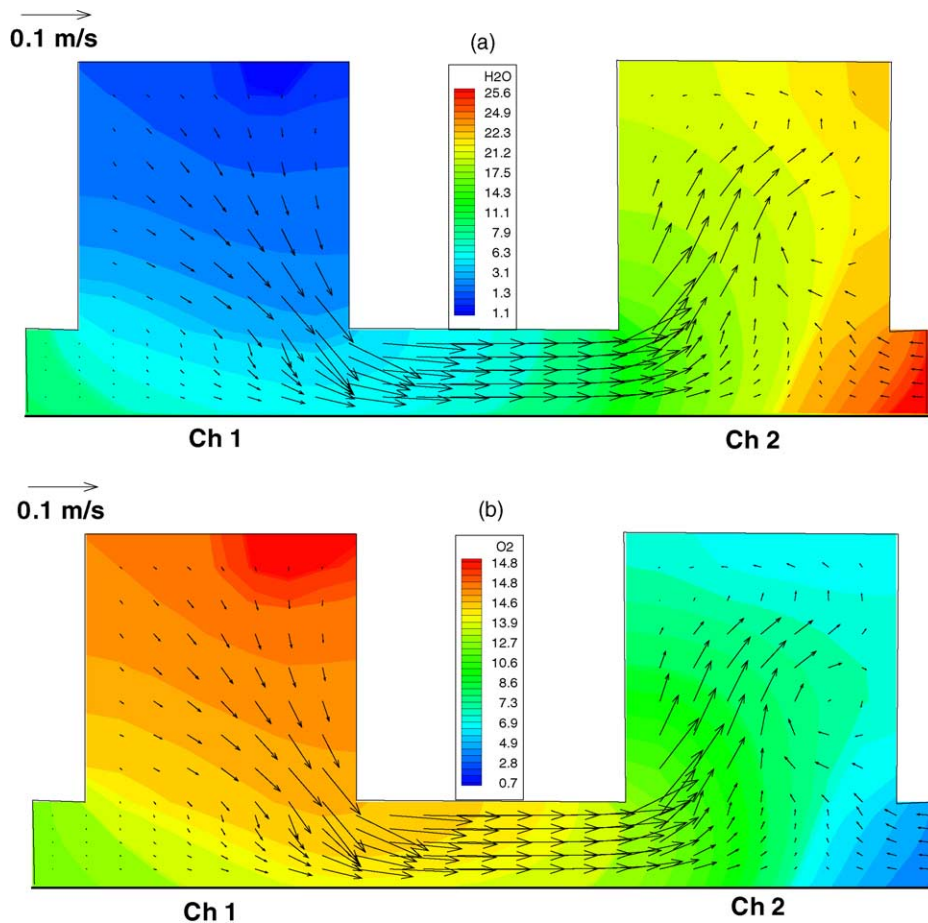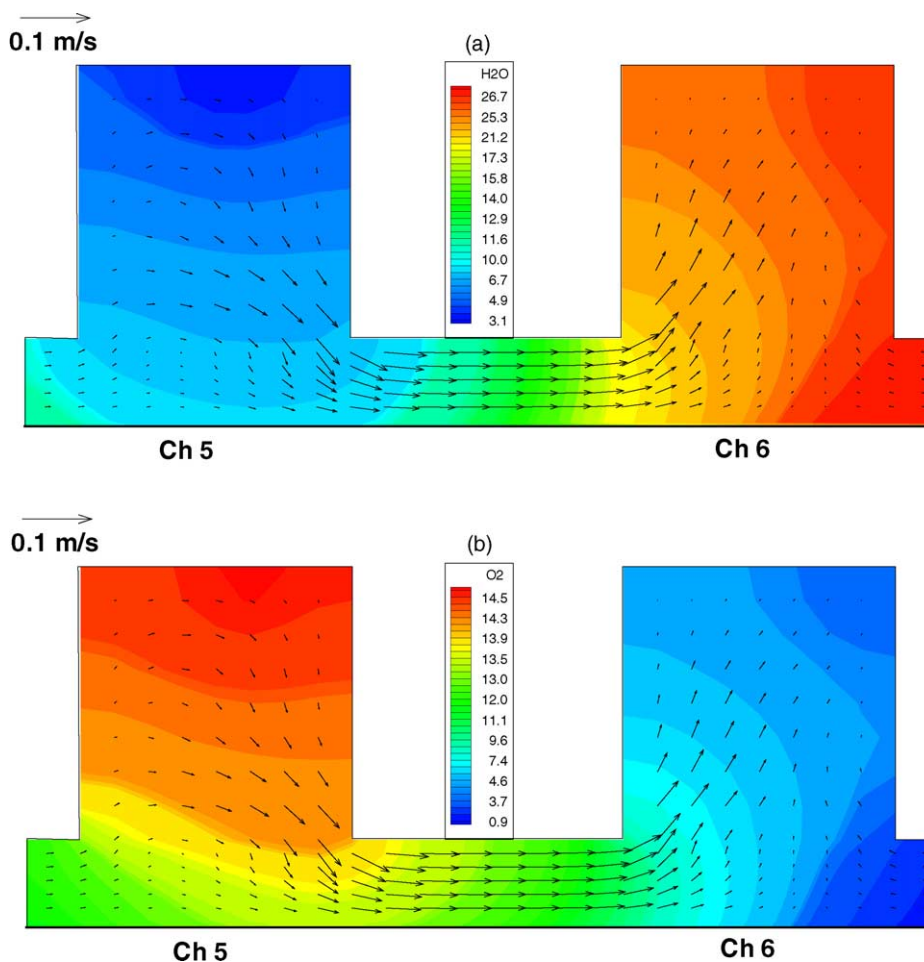

Fig. 10. (a) H$_2$O and (b) O$_2$ distributions and velocity in the cathode side at the mid-length cross-section between Channels 1 and 2 with convection in the GDL at $V_{\text{cell}} = 0.65$ V and $I_{\text{avg}} = 0.88$ A/cm^2.

Fig. 11. (a) H$_2$O and (b) O$_2$ distributions and velocity in the cathode side at the mid-length cross-section between Channels 5 and 6 with convection in the GDL at $V_{cell} = 0.65$ V and $I_{avg} = 0.88$ A/cm^2.
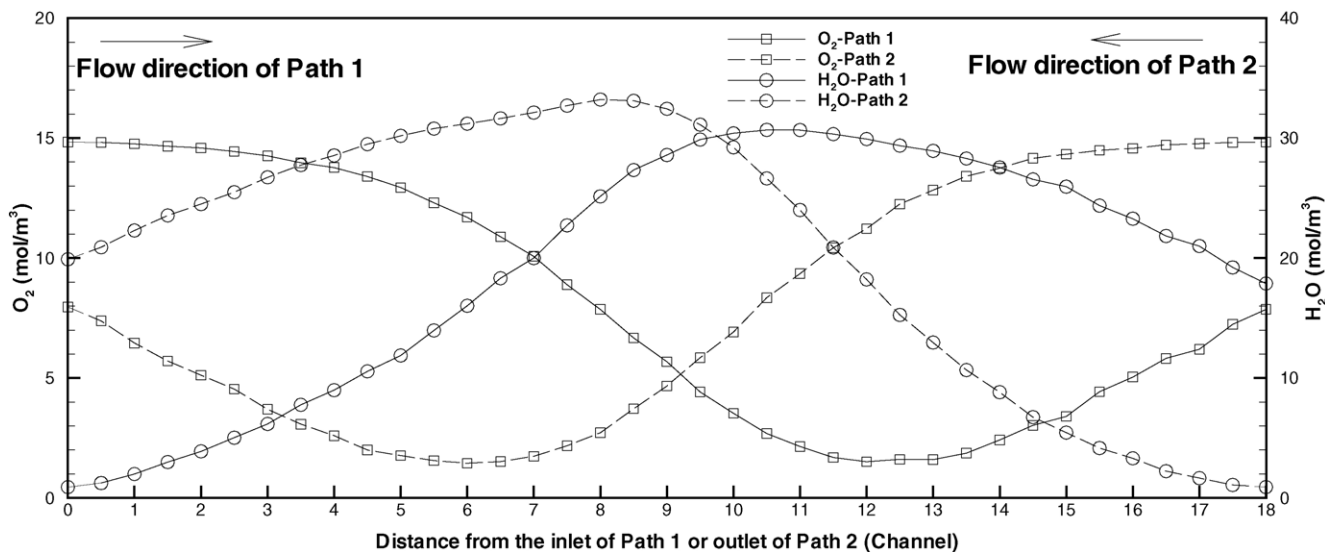

Fig. 12. Average H$_2$O/O$_2$ concentrations in the cathode gas channel for each flow path with convection in the GDL at $V_{cell} = 0.65$ V and $I_{avg} = 0.88$ A/cm^2.
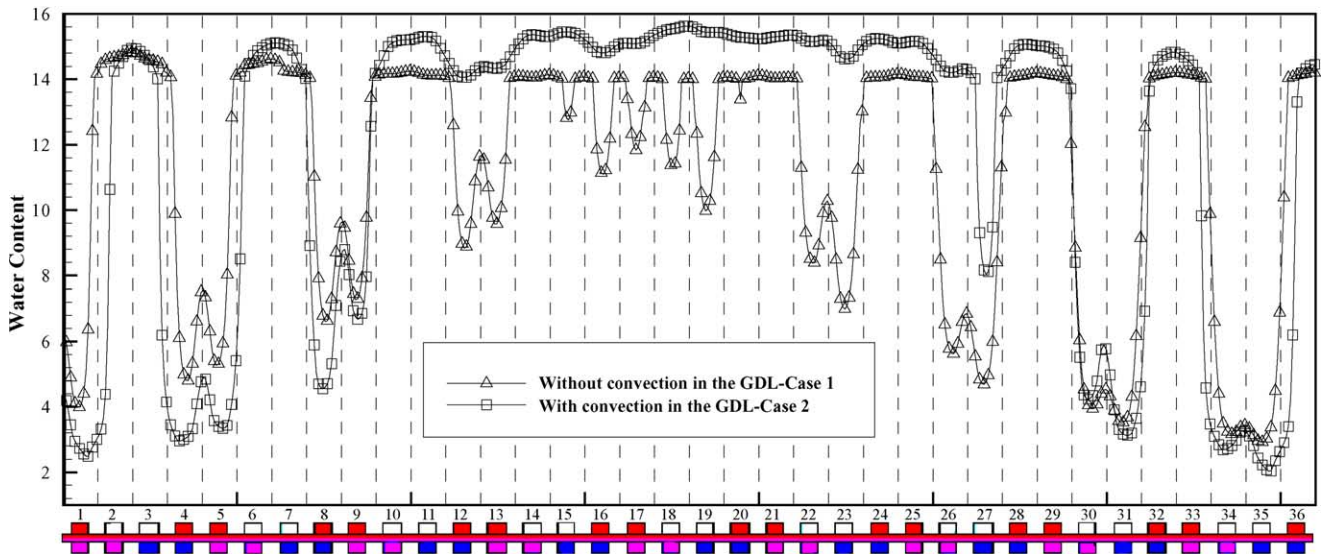
Fig. 13. Water content profile at the interface of the membrane and cathode catalyst layer at the mid-length cross-section.

An integral effect of gas bypass is shown in Fig. 12, which plots H_2O/O_2 concentrations in the cathode gas channel for each flow path. Contrary to Case 1, along each flow path, H_2O concentration increases first due to ORR water production but decreases later due to addition of drier gas from the other flow path. Furthermore, water concentration reaches as high as $30\,mol/m^3$ in the middle of the fuel cell, due partly to the deceleration of channel flow as shown in Fig. 9.

The trends of O_2 concentrations of the two flow paths are also different from Fig. 3. It is shown that O_2 concentration decreases first along the flow due to ORR consumption, then increases due to bypass of fresher air. In addition, high O_2 concentration at the outlet indicates that bypass causes a very serious leakage of O_2 and hence, lower cell performance in this case. Furthermore, because O_2 concentration becomes

very low, around $2\,mol/m^3$, in the middle of the flow field, O_2 transport limitation occurs and leads to low current density locally.

The benefit of self-humidification is best reflected by the membrane water content profile. Fig. 13 shows such profiles at the interface between the membrane and cathode catalyst layer for both cases. On the two ends of the fuel cell, it can be seen that the membrane hydration in Case 1 is better than Case 2 where internal humidification is suppressed by flow bypass.

Fig. 14 shows the current density distributions at the same cross-section. Focusing on the inlet Channels 1 and 35, it can be seen internal humidification increases the current density for Case 1, comparing to Case 2. In addition, bypass forces the dry air across the GDL between the adjacent inlet and
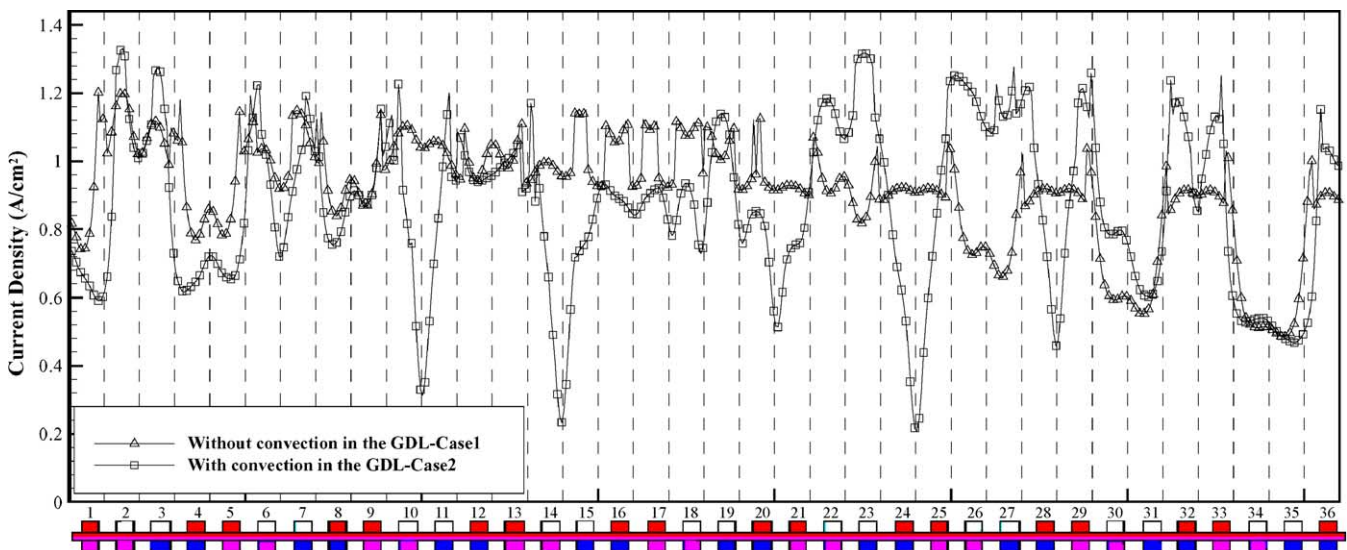

Fig. 14. Current density distribution profile at the mid-length cross-section.
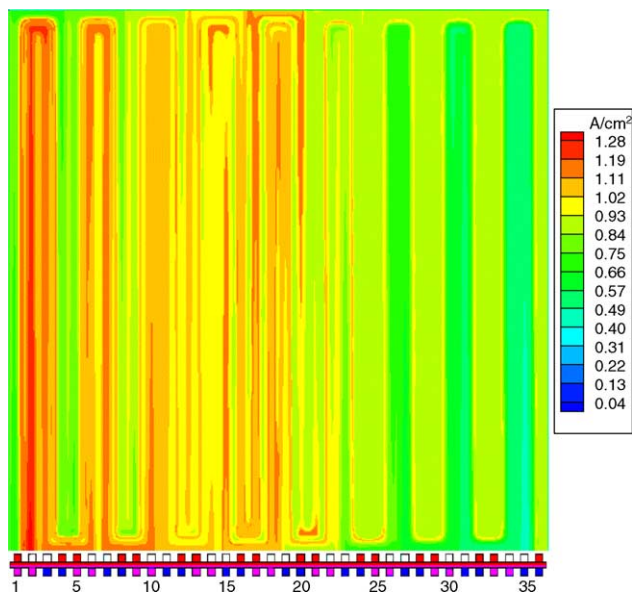
Fig. 15. Current density contours for Case 1 at $V_{cell} = 0.65$ V and $I_{avg} = 0.91$ A/cm^2.

outlet channels so that lower current density, resulting from higher ionic resistance, appears under the land in Case 2. As another result of bypass, higher current densities under Channels 2 and 36 are seen in Case 2 because O$_2$-rich air is added into these moisture channels by bypass. Meanwhile, there exist very low current densities under lands for Case 2, such as the land between Channels 14 and 15. This is because O$_2$ concentration reaches a low level, as shown in Fig. 12. Highly non-uniform current distribution is apparent from channel to channel in this flowfield.

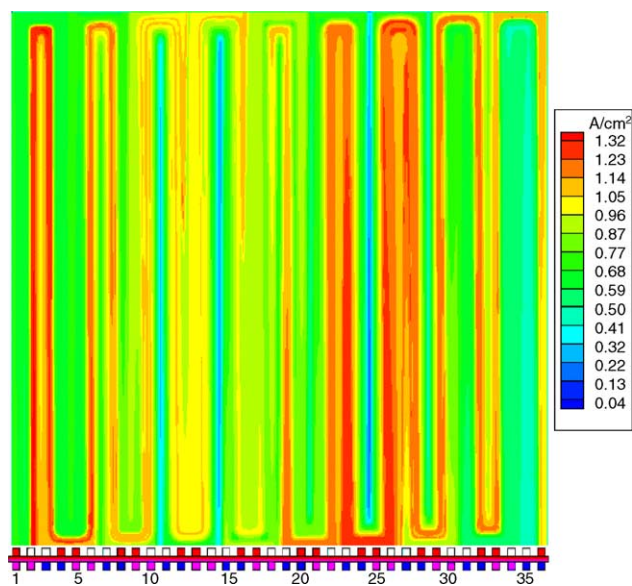Fig. 15 shows the current density contours for Case 1. This local performance of the PEFC is mainly determined by two factors, O$_2$ concentration and membrane hydration. The asymmetry of the distribution between the two counter flow paths on the cathode is remarkable, obviously due to the co-flow configuration of the anode where the anode inlet is always located on one side of the anode plate. In addition, the highest current density occurs near Channels 2 and 3 because these locations are near the wet cathode outlet and anode inlet. Under the inlet channels in cathode, such as Channels 1 and 35, the current density is low due to dry air injection. Along the flow path, the current density increases because water production and self-humidification raise the membrane hydration level. This trend is clearly shown in Path 2. For Path 1, more O$_2$ consumption near the inlet results in decreasing current density in the latter part of this flow path. Fig. 16 shows the current density contours for Case 2.

4. Conclusions

Numerical simulations of a double-path flowfield PEFC with 36 channels have been carried out to study the complex flow phenomena and water transport in PEFCs. The simulation results reveal that the effect of internal humidification induced by diffusion promoted by making the two neighboring channels in counter flow is significant, but is in reality offset by the opposed gas bypass flow induced also by the same flow configuration. In addition, the bypass phenomenon leads to significant leakage of gas, substantially reducing the reactant utilization. To decrease the effect of bypass, small permeability of GDLs was recommended for the double-path, counter-flow PEFCs.

While the counter flow between two neighboring flow paths in the same cathode flowfield is found ineffective through this extensive numerical study, this configuration provides a unique opportunity to explore the rich physics behind the complex flow and transport phenomena occurring in a PEFC as well as to test any numerical models of PEFCs.

Acknowledgements

Fig. 16. Current density contours for Case 2 at $V_{cell} = 0.65$ V and $I_{avg} = 0.88$ A/cm^2.

References

[1] M.L. Perry, T.F. Fuller, J. Electrochem. Soc. 149 (7) (2002) S59–S67.
[2] Z. Qi, A. Kaufman, J. Power Sources 109 (2002) 469–476.
[3] D.M. Bernardi, M.W. Verbrugge, J. Electrochem. Soc. 139 (1992) 2477–2491.
[4] T.E. Springer, T.A. Zawodinski, S. Gottesfeld, J. Electrochem. Soc. 136 (1991) 2334–2341.
[5] T.E. Springer, M.S. Wilson, S. Gottesfeld, J. Electrochem. Soc. 140 (1993) 3513–3527.
[6] T.F. Fuller, J. Newman, J. Electrochem. Soc. 140 (1993) 1218–1225.

[7] T.V. Nguyen, R.E. White, J. Electrochem. Soc. 140 (1993) 2178–2187.

[8] T. Berning, D.M. Lu, N. Djilali, J. Power Sources 106 (2002) 284–294.

[9] S. Dutta, S. Shimpalee, J.W. Van Zee, J. Appl. Electrochem. 30 (2000) 135–146.

[10] S. Dutta, S. Shimpalee, J.W. Van Zee, Int. J. Heat Mass Transfer 44 (2001) 2029–2042.

[11] S. Um, C.Y. Wang, K.S. Chen, J. Electrochem. Soc. 147 (2000) 4485–4493.

[12] S. Um, C.Y. Wang, Proceeding of the ASME Heat Transfer Division, vol. 1, Orlando, FL, 2000, p. 19.

[13] S. Um, C.Y. Wang, J. Power Sources 125 (2004) 40–51.

[14] H. Meng, C.Y. Wang, Chem. Eng. Sci. 104 (2004) 4727–4766.

[15] H. Meng, C.Y. Wang, J. Electrochem. Soc. 151 (2004) A358–A367.

[16] Y. Wang, C.Y. Wang, J. Electrochem. Soc. 152 (2005) A445–A453.

[17] S.V. Patankar, Numerical Heat Transfer and Fluid Flow, Hemisphere Publishing Corporation, New York, 1980.

[18] Y. Wang, C.Y. Wang, Electrochim. Acta 50 (2005) 1307–1315.

[19] S. Motupally, A.J. Becker, J.W. Weidner, J. Electrochem. Soc. 147 (2000) 3171–3177.

[20] T.A. Zawodzinski, J. Davey, J. Valerio, S. Gottesfeld, Electrochim. Acta 40 (1995) 297–302.

[21] A.C. West, T.F. Fuller, J. Appl. Electrochem. 26 (1996) 557.

[22] R.B. Bird, W.E. Stewart, E.N. Lightfood, Transport Phenomena, John Wiley & Sons, New York, 1960.

[23] F.P. Incropera, D.P. DeWitt, Fundamentals of Heat and Mass Transfer, John Wiley & Sons, New York, 1996.